Indonesian Journal of Science & Technology

Journal homepage: http://ejournal.upi.edu/index.php/ijost/

Activated Carbon Films from Water Hyacinth Waste for Stable and Sustainable Counter-Electrode Application in Dye-Sensitized Solar Cells

Roongroj Kamanja[1], Sawitree Wongrerkdee[1], Tipawan Rungsawang[2], Sutthipoj Wongrerkdee[2]*
Sucheewan Krobthong[2], Pichitchai Pimpang[3], Napat Kaewtrakulchai[4], Kanit Manatura[5]

[1]Rajamangala University of Technology Lanna Tak, Tak, Thailand
[2]Kasetsart University Kamphaeng Saen Campus, Nakhon Pathom, Thailand
[3]Pibulsongkram Rajabhat University, Phitsanulok, Thailand
[4]Kasetsart University, Bangkok, Thailand
[5]Rajamangala University of Technology Isan, Nakhon Ratchasima, Thailand
*Correspondence: E-mail: sutthipoj.s@gmail.com

ABSTRACT

This study explores the synthesis and application of water hyacinth-activated carbon (WHAC) as a counter-electrode in dye-sensitized solar cells (DSSCs). Characterization analyses, including X-ray diffraction, Raman spectroscopy, Fourier-transform infrared spectroscopy, and the N_2 adsorption-desorption isotherm, confirmed the polycrystalline and mesoporous nature of WHAC, whose pore size and surface area are 3.06 nm and 176.7 m^2/g, respectively. WHAC films deposited on the fluorine-doped tin oxide presented rough, random surface morphologies and thicknesses at higher concentrations. Optimized WHAC-based DSSCs presented a 1.40 ± 0.16% power conversion efficiency (PCE) compared to the 1.66 ± 0.26% presented by the standard platinum-based counter-electrodes. The efficiency improvement in the case of the WHAC-based DSSCs was the result of efficient electron transport, evident from the low sheet resistance and stable redox characteristics. The findings suggest WHAC is a promising and sustainable catalytic material for DSSC counter-electrodes.

ARTICLE INFO

Article History:
Submitted/Received 29 Nov 2024
First Revised 20 Dec 2024
Accepted 26 Feb 2025
First Available Online 27 Feb 2025
Publication Date 01 Apr 2025

Keyword:
A dye-sensitized solar cell,
Activated carbon,
Catalytic material,
Counter-electrode,
Film.

1. INTRODUCTION

Dye-sensitized solar cells (DSSCs) are compelling photovoltaic technology due to their simple fabrication and non-vacuum processing requirements. Conventional DSSCs consist of dye sensitizers, electrolytes, photo-electrodes (PEs), and counter-electrodes (CEs). The dye molecules in the embedded PEs are the major functional elements in light absorption, the generation of electron-hole pairs, and the transmission of electrons through the external load. The electrons, having traversed the external load, return to the DSSC through the catalytic activity of the CEs and participate in the redox reaction in the electrolyte to recharge the dye. Thus, the CEs are necessary electrocatalysts to provide a steady current. The conventional material for the CEs is the scarce and expensive platinum (Pt) due to its good catalytic activity and conductivity. However, the use of scarce and expensive Pt presents limitations in terms of mass-scale fabrication, and research continues to explore the use of cheaper and more available alternative materials. Recent developments have focused on alternative CE materials to enhance cost-effectiveness, sustainability, and mass production. Among these alternatives, carbon-based materials such as graphite, graphene, carbon nanotubes, carbon nanofibers, and activated carbon (AC) have emerged as attractive substitutes for Pt due to their excellent electrocatalytic properties, making them suitable candidates for counter-electrodes [1, 2].

Various natural organic carbon sources have been utilized for carbon-based CEs in DSSCs, demonstrating their effectiveness as viable alternatives to conventional Pt-based CEs. For instance, biochar, synthesized via pyrolysis from wood and corn silage, was combined with titanium isopropoxide (TTIP) to formulate biochar/TTIP inks [3]. These inks were then screen-printed to deposit biochar/TTIP hybrid CEs and fabricate DSSCs. Photovoltaic performance analysis revealed that DSSCs incorporating biochar/TTIP hybrid CEs exhibited higher power conversion efficiency (PCE) than those employing conventional Pt-based CEs. Similarly, conventional agricultural residues, such as corncob (CC), have been explored as carbon sources for CE fabrication. Corncob-derived carbon powder was integrated with the conductive polymer, poly(3,4-ethylenedioxythiophene): poly(styrenesulfonate) (PEDOT: PSS, PP) [4]. When deposited onto fluorine-doped tin oxide (FTO) substrates, the CC-PP composite exhibited enhanced redox reaction kinetics due to its superior conductivity and catalytic activity, resulting in a DSSC PCE of 5.85±0.87%, which surpassed the performance of Pt-based DSSCs (5.43±0.48%). In another approach, selenium (Se) was incorporated into porous AC derived from fruit peel waste to develop Se@AC CEs for DSSC applications [5]. The DSSCs utilizing Se@AC CEs achieved a PCE of 5.67%, approaching the efficiency of Pt-based DSSCs at 6.86%.

Water hyacinth (WH) (*Eichhornia crassipes*) is an invasive aquatic plant known for rapid growth and disruptive impact on the ecosystem, environment, and human activities. As an aquatic invader, WH also poses significant problems to water by consuming oxygen, plugging waterways, and causing local biodiversity disruption. Despite the ecological problems, WH presents a challenge for added-value applications because it contains a high carbon content, which, in turn, provides tremendous promise for use as source material in the synthesis of carbon-based products, most notably in environmental and energy applications. A major application of WH-based carbon products lies in environmental cleanup. Biochar derived from WH has been utilized for the removal of methylene blue, exhibiting a high adsorption capacity of 323 mg/g [6]. This performance is attributed to its large surface area, which enhances chemisorption, in line with the pseudo-second-order kinetic model. Another approach for WH-derived biochar synthesis involves hydrothermal pretreatment followed by molten salt

DOI: https://doi.org/10.17509/ijost.v10i1.80970
p- ISSN 2528-1410 e- ISSN 2527-8045

activation, resulting in a highly porous biochar with a surface area of 2240 m^2/g and a well-developed hierarchical pore structure [7]. These structural properties significantly enhance its adsorption and catalytic activity for peroxy disulfate (PDS) removal. For another application, WH-activated carbon (WHAC) has also demonstrated potential as an electrocatalyst in fuel cells [8]. While carbon-based CEs from natural sources (for example, biochar, crop residues, and fruit peels) have been studied, the use of WH-derived activated carbon (WHAC) as a CE material in DSSCs has received less research attention. The use of WHAC in adsorption and electrocatalysis applications has already shown catalytic activity in previous research, but its applications in electrochemical activity for DSSCs' CEs, despite prior studies, also lack thorough investigation. Additionally, the correlation between structure-based characteristics (carbon content, pore structure, and surface area) and their applications in electrochemical activity for the CE has not been adequately explored. In this study, the stem of WH waste was selected as a raw material to produce WHAC due to its high carbon content and surface area, potentially offering excellent catalytic properties for CE application.

2. METHODS

The synthesis of WHAC involved a sequential process starting with the hydrothermal of dried WH stem at a temperature of 500 °C to carbonize the WH, yielding a carbon-based material product. Subsequently, a chemical activation process utilizing KOH was employed, resulting in the formation of WHAC [9]. For practical application, WHAC was solubilized in acetone at different concentrations of 0.01, 0.05, and 0.10 g/mL and stirred for an hour to ensure a uniform WHAC solution. Then, 30 µL of the WHAC solution was dropped and dispensed onto a cleaned FTO substrate, within an active area of 1 cm^2. This deposition process was repeated after drying. The deposited WHAC underwent heat treatment at 200 °C for 3 hours, resulting in the formation of compact WHAC films. These films were then employed as CEs in ZnO-based DSSCs. For comparison, a conventional Pt CE was prepared using 0.05 M H2PtCl6·6H2O (Merck, ACS reagent) in acetone, dropped onto FTO (7 Ω/sq, Greatcell Solar Materials) substrates, and sintered at 550 °C for 1 hour.

In the DSSC fabrication process, 5 g of ZnO powder (Merck, <5 µm) was mixed with 12 mL of 10 vol.% ethylene glycol in distilled water. The mixture was stirred at room temperature for an hour, resulting in ZnO paste. Subsequently, the ZnO paste was screen-printed onto a 1 cm^2 active area FTO substrate and annealed at 400 °C for an hour, producing ZnO films. The films were then immersed in a solution containing N719 dye (Greatcell Solar Materials) dissolved in acetonitrile (0.3 mM). The immersion process followed a re-adsorption method described elsewhere to obtain the ZnO photo-electrode [10]. Next, the photo- and counter-electrodes were assembled in a sandwich configuration using a polymer. In the final step, electrolyte (EL-HPE, Greatcell Solar Materials) was injected into the space between the photo- and counter-electrodes. Photovoltaic characteristics were immediately measured under simulated sunlight at a standard intensity of 100 mW/cm^2.

The crystallite structures were examined using an X-ray diffractometer (XRD; Rigaku, SmartLab), while the graphitic structures of WHAC were analyzed with a Raman spectrophotometer (Thermo Scientific, DXR SmartRaman). Surface functional groups were monitored using Fourier transform infrared (FTIR) spectroscopy (PerkinElmer, Spectrum Two). The N_2 adsorption-desorption method was conducted with a surface area and pore size analyzer (Quantachrome, Autosorb iQ-C-XR-XR-XR) to gain insights into porosity properties. Morphology was observed through a scanning electron microscope (SEM), and the sheet resistance was measured using a four-point probe system (Ossila). The redox characteristics

DOI: https://doi.org/10.17509/ijost.v10i1.80970
p- ISSN 2528-1410 e- ISSN 2527-8045

of the WHAC CEs were evaluated using cyclic voltammetry (CV) at room temperature, with measurements conducted using an Autolab PGSTAT204 electrochemical station (Metrohm).

3. RESULTS AND DISCUSSION

The crystallite structures of water hyacinth-activated carbon (WHAC) were investigated using XRD. The XRD results revealed several detectable peaks, with carbon-related peaks assigned and labeled in **Figure 1** (JCPDS no. 20-0258) [11]. Notably, the peak at 2θ of around 28.3° could correspond to graphitic structures [12]. The other unclear patterns, characterized by a lack of distinct and well-defined diffraction patterns, suggest the presence of polycrystalline structures, referring to numerous small and randomly oriented crystallites in the synthesized WHAC sample. These characteristics may indicate the presence of numerous grain boundaries, defects, and impurities.

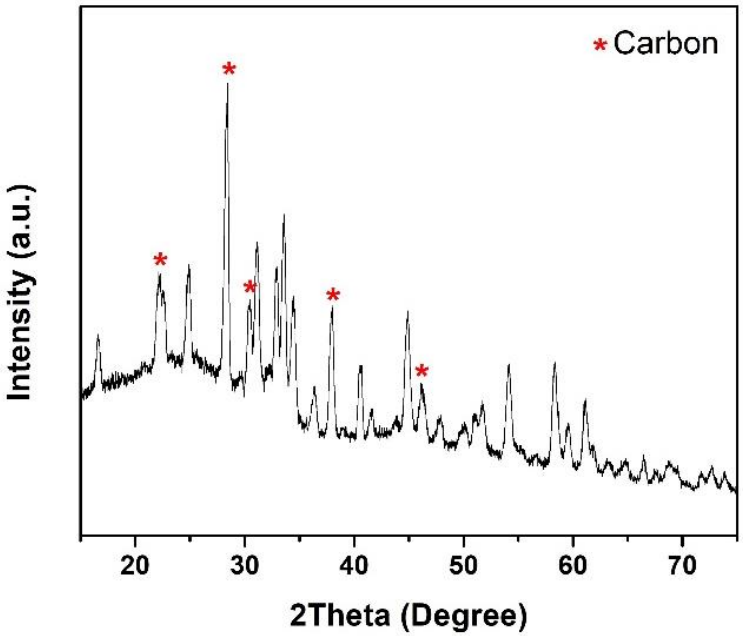

Figure 1. X-ray diffraction pattern analysis of WHAC.

Raman spectroscopy, as shown in **Figure 2(a)**, reveals two distinctive peaks located at 1362 and 1592 cm^{-1}, attributing the sp^3 lattice defects to the disordered (D) peak and sp^2 carbon atoms to the graphitic (G) peaks, respectively. The D peak indicates disordered structures, while the G peak represents well-ordered graphitic carbon structures. To investigate the level of disorder in the synthesized WHAC, the intensity ratio of the D peak to the G peak (I_D/I_G) was calculated. A high I_D/I_G ratio of 2.8 was obtained, implying a high degree of disorder. This result indicates significant amorphous structures in the synthesized WHAC, aligning with the XRD analysis. Moreover, this finding is consistent with the FTIR spectra of functional group analysis shown in **Figure 2(b)**. Prominent FTIR peaks were observed at wavenumbers of 1740, 1365, 1217, and 1017 cm^{-1}, which are related to carbon bonding for all wavenumbers [13]. The peak at 1740 cm^{-1} typically corresponds to C=O stretching vibrations. The peak at 1365 cm^{-1} may indicate C–H bending vibration, while the two peaks at 1217 and 1017 cm^{-1} are associated with C–O stretching vibrations [14, 15]. These observed peaks suggest that the major structures of carbon involve oxygen and hydrogen compounds.

DOI: https://doi.org/10.17509/ijost.v10i1.80970
p- ISSN 2528-1410 e- ISSN 2527-8045

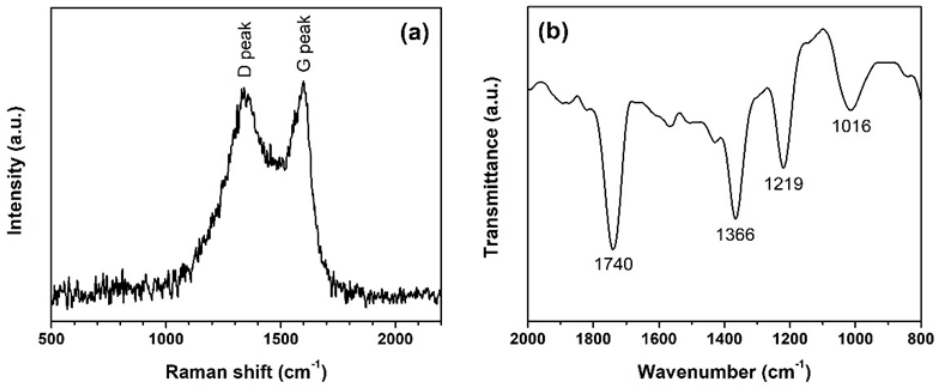

Figure 2. Vibrational analysis of WHAC: (a) Raman spectroscopy and (b) FTIR.

A non-destructive analysis using the N2 adsorption-desorption method was conducted to determine the porosity property of WHAC, as shown in **Figure 3**. **Figure 3(a)** shows that the N2 adsorption-desorption isotherm exhibited an H3 hysteresis loop, indicative of mesoporous structures. This finding aligns with the average pore diameter of 3.06 nm, as analyzed in **Figure 3(b)** using the Barrett-Joyner-Halenda (BJH) adsorption method. Furthermore, a high surface area of 176.7 m2/g was estimated using the Brunauer-Emmett-Teller (BET) method. The mesoporous nature of WHAC suggests a well-defined and interconnected porous network, making it particularly relevant for applications such as adsorbents, gas separators, and catalysts. In this research, the potential application of WHAC as a catalyst, substituting the conventional Pt CEs in DSSCs, was demonstrated.

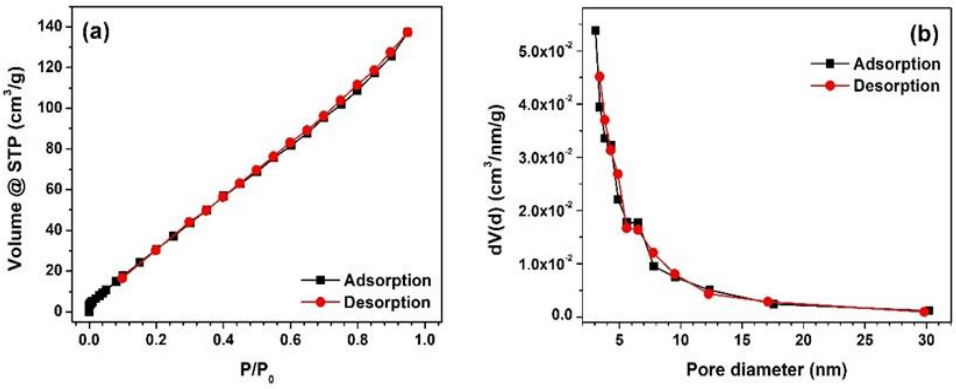

Figure 3. Porosity analysis of WHAC: (a) N_2 adsorption-desorption isotherm, (b) pore diameter distribution.

The morphology of CEs prepared from three different WHAC conditions of 0.01, 0.05, and 0.10 g/mL, as labeled to be WHAC01, WHAC05, and WHAC10, respectively, is presented in **Figure 4(a-c)**. The morphological structures exhibit random-rough surfaces, which could be attributed to differences in sizes, shapes, and orientations of WHAC particles. In **Figure 4(d-f)**, cross-sectional SEM images were used to measure thickness. The average thickness of the WHAC CEs is 12.76, 41.90, and 70.86 μm for WHAC01, WHAC05, and WHAC10, respectively. The thickness exhibited an increasing trend with increasing concentrations, due to the larger amount of WHAC used. The increased thickness also reduced the sheet resistance of WHAC CEs, as presented in **Figure 5**. This suggests good carrier conduction through the WHAC, potentially enhancing electron collection from external loads and facilitating redox reductions to complete the electronic cycle in DSSCs.

DOI: https://doi.org/10.17509/ijost.v10i1.80970
p- ISSN 2528-1410 e- ISSN 2527-8045

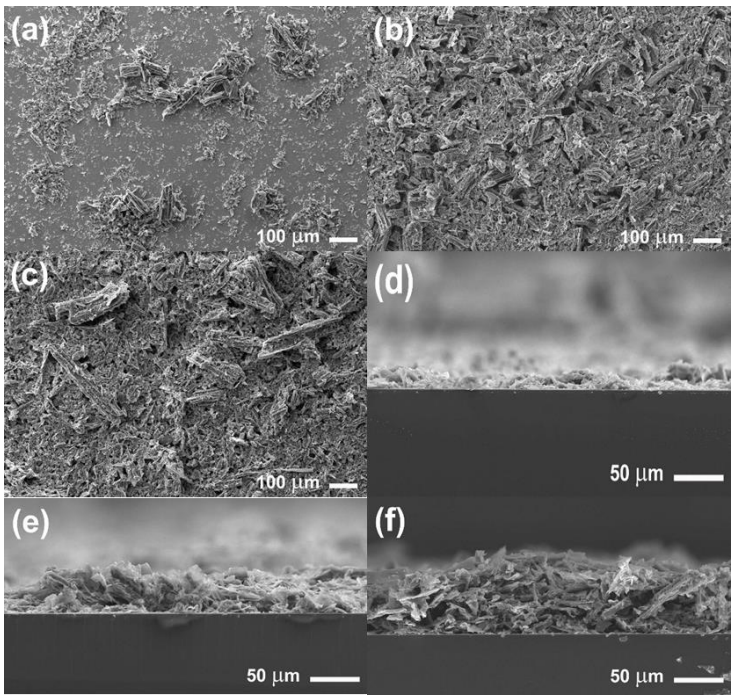

Figure 4. SEM image analysis: morphology of (a) WHAC01, (b) WHAC05, and (c) WHAC10; cross-sectional image of (d) WHAC01, (e) WHAC05, and (f) WHAC10.

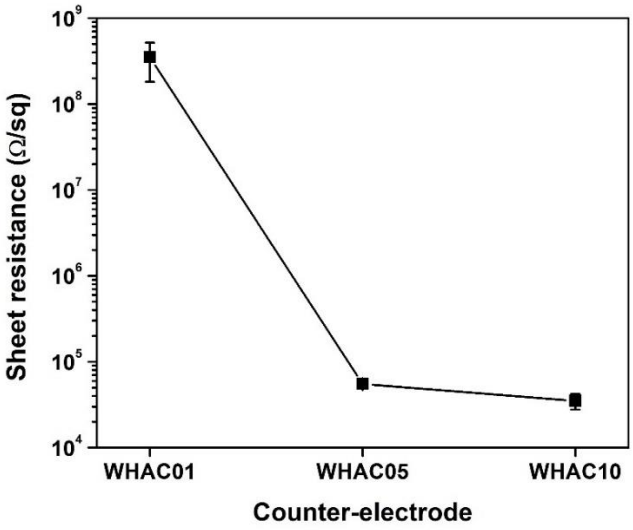

Figure 5. The sheet resistance of different WHAC counter-electrodes.

In the analysis of redox characteristics, three different conditions were observed: FTO glasses, Pt-coated FTO glasses, and WHAC10-coated FTO glasses. Cyclic voltammetry (CV) involves applying a voltage waveform and monitoring the resulting current response, as presented in **Figure 6**. The potential range for the measurement was set from -1.0 V to 1.0 V, with a potential scan rate of 0.05 V/s, and each condition was scanned three times. In the study, three different types of electrodes were utilized: the conductive films, Pt, and Ag/AgCl, serving as the working, counter, and reference electrodes, respectively. CV curves typically display two distinct regions: the anodic region (positive current values) and the cathodic region (negative current values). These regions correspond to the oxidation and reduction reactions, respectively, occurring at the working electrode surface. A 0.1 M KCl solution (99.5%, Loba Chemie) was used as the electrolyte, providing an ionic medium for the

DOI: https://doi.org/10.17509/ijost.v10i1.80970
p- ISSN 2528-1410 e- ISSN 2527-8045

electrochemical reactions during the cyclic voltammetry measurements [16-17]. **Figure 6(a)** illustrates the CV measurements of FTO glasses. The CV result shows cathodic peak potential (E_c) at approximately -0.6 V, suggesting the reduction potential of FTO. It appears that the current decreased in the 2nd and 3rd loops, indicating the electrochemical etching of the FTO film and suggesting unstable redox characteristics. **Figure 6(b)** reveals the CV measurements of Pt-coated FTO glasses. In the 1st loop, the E_c peaks were observed at around -0.1 V and -0.6 V, indicating the reduction potentials of Pt and FTO, respectively. In the 2nd and 3rd loops, the E_c peaks of Pt and FTO decrease, but a new peak appears at approximately -0.3 V, suggesting the presence of a new chemical composition. **Figure 6(c)** explores the CV measurements of WHAC10-coated FTO glasses. It appears that the CV curves have similar patterns, indicating that WHAC10 exhibits stable redox characteristics and is resistant to changes in its electrochemical behavior. This behavior can improve the stability of DSSCs fabricated with WHAC-based CEs.

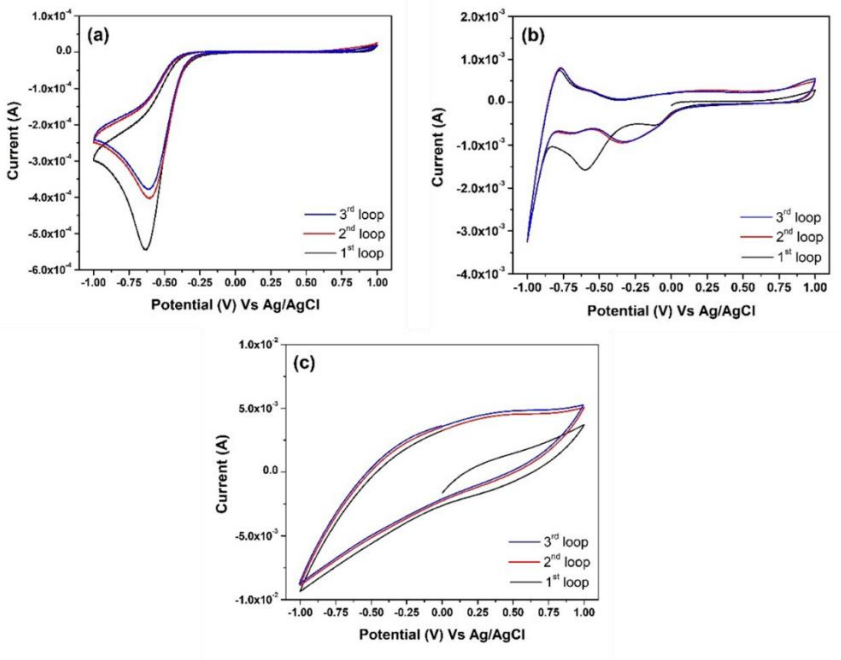

Figure 6. The CV measurements of the conductive films under three different conditions: (a) FTO glasses, (b) Pt-coated FTO glasses, and (c) WHAC10-coated FTO glasses.

To investigate the utilization of WHAC CEs in DSSCs, the current density (J) versus voltage (V) characteristics were measured under simulated solar irradiation, as illustrated in **Figure 7**. The J-V measurements of DSSCs were conducted with at least three repeated samples for each condition to ensure statistical reliability and minimize experimental variations. The results demonstrated that the thickness of the WHAC CEs exhibits a direct correlation with the short-circuit current density (J_{sc}), whereas the open-circuit voltage (V_{oc}) shows only slight variation across different CE thicknesses. J_{sc} is considered a significant determining factor in the efficiency of the DSSC. The dependence of the thickness of the WHAC CE on J_{sc} suggests that the greater the thickness of the WHAC layer, the greater the available sites for the reduction of I_3^- to I^- in the electrolyte, and the greater the efficiency in the transfer and transport of charge. The V_{oc}, representing the difference in potentials at zero current, remained the same at various thicknesses of the CE. This suggests that WHAC only affects charge transport and not the energy shift in the energy levels of the redox couple, given that V_{oc} is dominated by the difference in the Fermi level between ZnO and the redox electrolyte.

DOI: https://doi.org/10.17509/ijost.v10i1.80970
p- ISSN 2528-1410 e- ISSN 2527-8045

In analyzing the performance of DSSCs, photovoltaic parameters were calculated using equations (1) and (2) [10, 18-19]:

$$PCE\ (\%) = (J_{sc} \times V_{oc} \times FF \times 100) / P_{in} \quad (1)$$

$$FF = P_{mp} / (J_{sc} \times V_{oc}) \quad (2)$$

Where PCE, FF, and P_{in} are the power conversion efficiency, fill factor, and incident simulated sunlight power, respectively. The calculated parameters shown in **Table 1** and plotted in **Figure 8** explore the impact of WHAC CEs on each photovoltaic parameter.

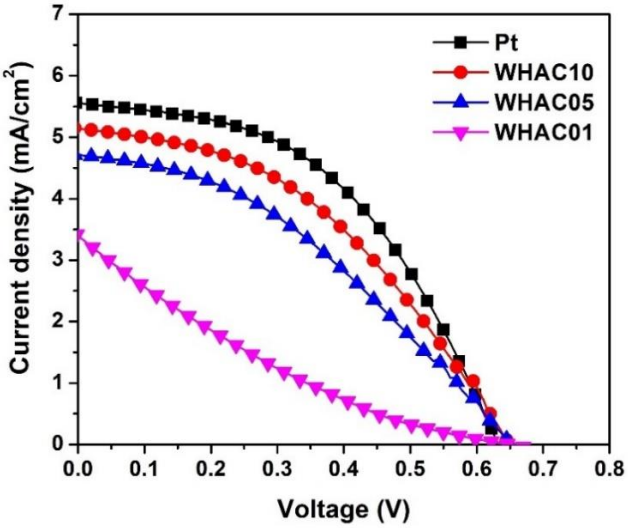

Figure 7. J-V curves of DSSCs fabricated with different counter-electrodes.

Figure 8(a) shows that J_{sc} increases with the concentration of WHAC, implying a crucial role in enhancing overall PCE. A similar trend is observed for FF in **Figure 8(c)**, indicating improved charge extraction and transport efficiency. The simultaneous increase in J_{sc} and FF is directly correlated with the enhanced PCE, as depicted in **Figure 8(d)**. Meanwhile, **Figure 8(b)** demonstrates that V_{oc} remains relatively stable under all conditions. The analysis explores a strong correlation between PCE and key photovoltaic parameters particularly J_{sc} and FF, while V_{oc} remains a neutral factor. To evaluate the resistance characteristics, R_s and R_{sh} values of DSSC devices were analyzed. **Figure 8(e)** demonstrates a strong decrease in R_s with increasing WHAC concentration, indicating better catalytic activity at higher WHAC content in the CEs. In contrast, **Figure 8(f)** shows that R_{sh} initially increases from WHAC01 to WHAC05, slightly decreases for WHAC10, and then rises again for Pt. Generally, a high R_{sh} signifies a reduced recombination effect due to faster charge transport. This is attributed to the concurrent reduction in R_s and increase in R_{sh}, thereby synergistically facilitating better catalytic activity and faster charge transport in DSSCs. The key improvement in PCE for DSSCs employing WHAC as the CEs is the thickness of the WHAC. In overall PCE considerations, the DSSCs fabricated with the WHAC10 CE display a notable enhancement in PCE, closely approaching that achieved with a Pt CE. Consequently, the results demonstrate the potential of WHAC as a promising alternative catalytic material for CE applications in DSSCs, offering a viable substitute for conventional Pt. In comparison with other reports, PCEs of ZnO photoelectrode (PE) DSSCs, fabricated with different carbon-based CEs, are summarized in **Table 2**. It was observed that the present study exhibited a lower PCE, potentially attributed to various factors such as preparation techniques, material quality, and equipment. Despite the lower

DOI: https://doi.org/10.17509/ijost.v10i1.80970
p- ISSN 2528-1410 e- ISSN 2527-8045

PCE observed in ZnO-based DSSCs fabricated with WHAC CEs, this work is noteworthy for introducing the utilization of WH waste as a value-added material in DSSCs. Additionally, the transformation and utilization of WHAC also contribute to the mitigation of carbon emissions by preventing the natural decomposition of WH waste.

Table 1. Photovoltaic parameters of DSSCs fabricated with different counter-electrodes.

CE	J_{sc} (mA/cm^2)	V_{oc} (V)	FF	PCE (%)	R_s (Ω)	R_{sh} (Ω)
WHAC01	3.50±0.20	0.66±0.01	0.20±0.01	0.45±0.02	109.6±3.2	546.2±74.8
WHAC05	4.71±0.73	0.65±0.02	0.38±0.02	1.16±0.20	83.2±16.2	842.3±68.3
WHAC10	5.15±0.61	0.65±0.01	0.42±0.01	1.40±0.16	59.8±0.5	738.2±62.0
Pt	5.56±1.64	0.63±0.02	0.48±0.05	1.66±0.26	39.7±1.2	897.3±175.1

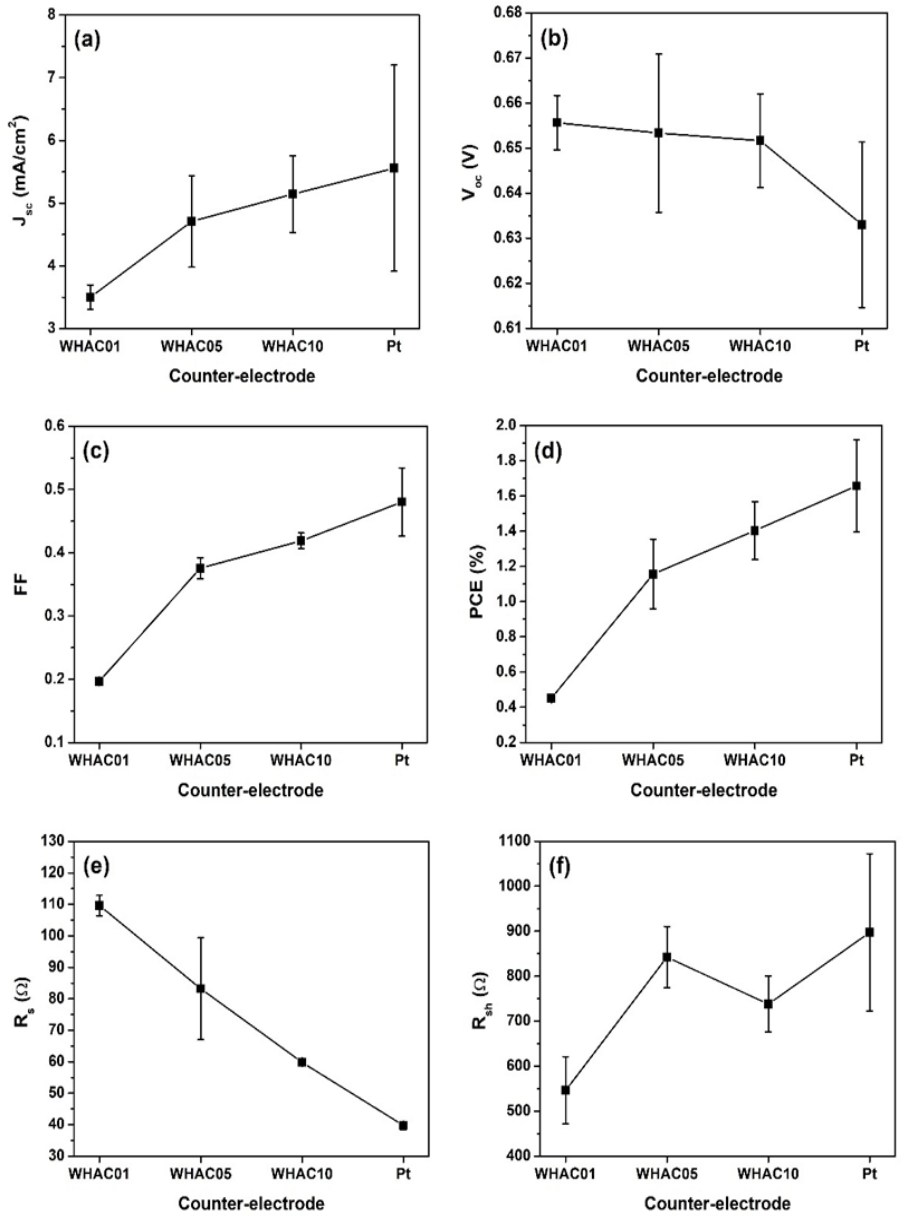

Figure 8. Plots of photovoltaic parameters of DSSCs fabricated with different CEs: (a) J_{sc}, (b) V_{oc}, (c) FF, (d) PCE, (e) R_s, and (f) R_{sh}.

DOI: https://doi.org/10.17509/ijost.v10i1.80970
p- ISSN 2528-1410 e- ISSN 2527-8045

Table 2. Comparative PCE of DSSCs fabricated with different carbon-based counter electrodes.

PE	Dye	EL	CE	PCE (%)
ZnO-G [20]	N749	I^-/I^{3-}	G	2.26
			MWCNTs	2.04
ZnO [21]	N749	I^-/I^{3-}	Pt/MWCNTs	3.78
			MWCNTs	2.26
ZnO [22]	N719	I^-/I^{3-}	G/MWCNTs	4.10
ZnO [23]	N719	I^-/I^{3-}	Co-Mo/carbon	4.81
ZnO (This work)	N719	I^-/I^{3-}	WHAC	1.40

G: graphene, MWCNTs: multi-walled carbon nanotubes, Co: cobalt, Mo: molybdenum.

4. CONCLUSION

WH waste was utilized as the raw material to synthesize WHAC using a hydrothermal process and activation with KOH. Characterization analyses, including XRD, Raman spectroscopy, FTIR, and N_2 adsorption-desorption isotherm, explored the polycrystalline structures of mesoporous carbon material. The WHAC was then coated on FTO substrates to prepare WHAC films at varying concentrations of 0.01, 0.05, and 0.10 mg/mL. The morphology of the WHAC films shows similar random rough surfaces; however, their thickness increased with increasing concentrations. These films were beneficially applied as catalytic CEs in DSSCs. The PCE of DSSCs fabricated with WHAC CEs was comparable to that of conventional Pt CEs. The observed improvements in PCE are directly dependent on the thickness of the WHAC films, with the facilitating role of electron transport aligning with the observed low sheet resistance. This contributes to the concurrent increase in R_{sh} and reduction in R_s, thereby synergistically enhancing electron transport efficiency in DSSCs. Moreover, the stable redox characteristics also improve the stability performance of DSSC devices. This study demonstrates that WHACs have acceptable potential to be applied as an alternative catalytic material for CE applications in DSSCs. Furthermore, it may be considered for other applications based on its porous catalytic properties, such as adsorbents and separators.

5. ACKNOWLEDGMENT

The authors would like to acknowledge the Department of Electrical Engineering, Faculty of Engineering, Rajamangala University of Technology Lanna Tak; the Department of Physical and Material Sciences, Faculty of Liberal Arts and Science, Kasetsart University Kamphaeng Saen Campus; and the Faculty of Science and Technology, Pibulsongkram Rajabhat University for facilities.

6. AUTHORS' NOTE

The authors declare that there is no conflict of interest regarding the publication of this article. The authors confirmed that the paper was free of plagiarism.

7. REFERENCES

[1] Samantaray, M. R., Mondal, A. K., Murugadoss, G., Pitchaimuthu, S., Das, S., Bahru, R., and Mohamed, M. A. (2020). Synergetic effects of hybrid carbon nanostructured counter electrodes for dye-sensitized solar cells: A review. *Materials, 13*(12), 2779.

[2] Wu, J., Lan, Z., Lin, J., Huang, M., Huang, Y., Fan, L., Luo, G., Lin, Y., Xie, Y., and Wei, Y. (2017). Counter electrodes in dye-sensitized solar cells. *Chemical Society Reviews, 46*(19), 5975–6023.

[3] Buchlová, T., Hatala, M., Veteška, P., Ház, A., Novák, P., Mackuľak, T., Mikula, M., and Gemeiner, P. (2024). Screen-printed counter-electrodes based on biochar derived from wood-corn silage and titanium isopropoxide binder as a more efficient and renewable alternative to Pt-CE for dye-sensitized solar cells. *Materials Science in Semiconductor Processing, 171*, 108016.

[4] Kanjana, N., Maiaugree, W., Tontapha, S., Laokul, P., Chingsungnoen, A., Pimanpang, S., Chaiya, I., Daengsakul, S., and Amornkitbamrung, V. (2023). Effect of carbonization temperature on the electrocatalytic property and efficiency of dye-sensitized solar cells derived from corncob and sugarcane leaf agricultural residues. *Biomass Conversion and Biorefinery, 13*, 8361–8371.

[5] Akman, E., and Karapinar, H. S. (2022). Electrochemically stable, cost-effective, and facile produced selenium@activated carbon composite counter electrodes for dye-sensitized solar cells. *Solar Energy, 234*, 368–376.

[6] Carneiro, M. T., Morais, A. Í. S., de Carvalho Melo, A. L. F., Ferreira, F. J. L., Santos, F. E. P., Viana, B. C., Osajima, J. A., Bezerra, R. D. S., Del Mar Orta Cuevas, M., Peña-Garcia, R. R., Almeida, L. C., and Silva-Filho, E. C. (2023). Biochar derived from water hyacinth biomass chemically activated for dye removal in aqueous solution. *Sustainability, 15*(19), 14578.

[7] Lu, L., Tang, D., Luo, Z., Mo, H., Sun, Y., Hu, J., and Sun, J. (2024). Water hyacinth derived hierarchical porous biochar absorbent: Ideal peroxydisulfate activator for efficient phenol degradation via an electron-transfer pathway. *Environmental Research, 242*, 117773.

[8] Morales, S. L., Baas-López, J. M., Barbosa, R., Pacheco, D., and Escobar, B. (2021). Activated carbon from water hyacinth as electrocatalyst for oxygen reduction reaction in an alkaline fuel cell. *International Journal of Hydrogen Energy, 46*(51), 25995–26004.

[9] Kaewtrakulchai, N., Faungnawakij, K., and Eiad-Ua, A. (2020). Parametric study on microwave-assisted pyrolysis combined KOH activation of oil palm male flowers derived nanoporous carbons. *Materials, 13*(12), 2876.

[10] Wongrerkdee, S., Moungsrijun, S., Pimpang, P., Hongsith, K., and Choopun, S. (2021). Linking bridge improvement of ZnO/N719 interfaces via ammonia treatment for efficiency enhancement of dye-sensitized solar cell. *Surfaces and Interfaces*, *23*, 100991.

[11] Maulina, W., Kusumaningtyas, R., Rachmawati, Z., Supriyadi, Arkundato, A., Rohman, L., and Purwandari, E. (2019). Carbonization process of water hyacinth as an alternative renewable energy material for biomass cookstoves applications. *IOP Conference Series: Earth and Environmental Science, 239*, 012035.

[12] Masakul, P., Nilmoung, S., Sonsupap, S., and Laorach, L. (2023). The electrochemical properties of water hyacinth-derived activated carbon. *Journal of Metals, Materials and Minerals, 33*(3), 1618.

DOI: https://doi.org/10.17509/ijost.v10i1.80970
p- ISSN 2528-1410 e- ISSN 2527-8045

[13] Nandiyanto, A. B. D., Oktiani, R., and Ragadhita, R. (2019). How to read and interpret FTIR spectroscope of organic material. *Indonesian Journal of Science and Technology, 4*(1), 97–118.

[14] Algarni, T. S., Al-Mohaimeed, A. M., Al-Odayni, A. B., and Abduh, N. A. Y. (2022). Activated carbon/$ZnFe_2O_4$ nanocomposite adsorbent for efficient removal of crystal violet cationic dye from aqueous solutions. *Nanomaterials, 12*(18), 3224.

[15] Gaitán-Alvarez, J., Berrocal, A., Mantanis, G. I., Moya, R., and Araya, F. (2020). Acetylation of tropical hardwood species from forest plantations in Costa Rica: An FTIR spectroscopic analysis. *Journal of Wood Science, 66*, 49.

[16] Wongrerkdee, S., and Pimpang, P. (2022). Fluorescence Quenching Probe Based on Graphene Quantum Dots for Detection of Copper Ion in Water. *Integrated Ferroelectrics*, *222*, 56–68.

[17] Wongrerkdee, S., Choopun, S., and Pimpang, P. (2023). Electrical and water resistance properties of conductive paste based on gold/silver composites. *Journal of Metals, Materials and Minerals*, *33*(4), 1786.

[18] Kanjana, N., Maiaugree, W., Laokul, P., Chaiya, I., Lunnoo, T., Wongjom, P., Infahsaeng, Y., Thongdang, B., and Amornkitbamrung, V. (2023). Fly ash boosted electrocatalytic properties of PEDOT: PSS counter electrodes for the triiodide reduction in dye-sensitized solar cells. *Scientific Reports, 13*, 6012.

[19] Krobthong, S., Nilphai, S., Choopun, S., and Wongrerkdee, S. (2020). Synthesis and characterization of ZnO nanoparticle films and its application in dye-sensitized solar cells. *Digest Journal of Nanomaterials and Biostructures, 15*(3), 885–894.

[20] Siwach, B., Mohan, D., Singh, K. K., and Kumar, A. (2018). Effect of carbonaceous counter electrodes on the performance of ZnO-graphene nanocomposites-based dye sensitized solar cells. *Ceramics International, 44*(17), 21120–21126.

[21] Siwach, B., Mohan, D., and Barala, M. (2019). Fabrication and characterization of MWCNTs and Pt/MWCNTs counter electrodes for dye sensitized solar cells. *AIP Conference Proceedings, 2142*(1), 050003.

[22] Wahyuono, R. A., Jia, G., Plentz, J., Dellith, A., Dellith, J., Herrmann-Westendorf, F., Seyring, M., Presselt, M., Andrä, G., Rettenmayr, M., and Dietzek, B. (2019). Self-assembled graphene/MWCNT bilayers as platinum-free counter electrode in dye-sensitized solar cells. *ChemPhysChem, 20*(24), 3336–3345.

[23] Shi, H., Xie, Y., Wei, P., Chen, H., and Qiang, Y. (2020). Application of Co-Mo bimetal/carbon composite in dye-sensitized solar cells and its research on synergy mechanism. *Journal of Solid-State Electrochemistry, 24*, 753–759.

DOI: https://doi.org/10.17509/ijost.v10i1.80970
p- ISSN 2528-1410 e- ISSN 2527-8045